ACSNANO
www.acsnano.org
ARTICLE

# Supra-Nanoparticle Functional Assemblies through Programmable Stacking

Cheng Tian,[†] Marco Aurelio L. Cordeiro,[†] Julien Lhermitte,[†] Huolin L. Xin,[†] Lior Shani,[‡] Mingzhao Liu,[†] Chunli Ma,[†] Yosef Yeshurun,[‡] Donald DiMarzio,[§] and Oleg Gang*[,†,∥,⊥]

[†]Center for Functional Nanomaterials, Brookhaven National Laboratory, Upton, New York 11973, United States

[‡]Department of Physics and Institute of Nanotechnology and Advanced Materials, Bar-Ilan University, 52900 Ramat-Gan, Israel

[§]NexGen - Next Generation Engineering, Northrop Grumman Corporation, One Space Park, Redondo Beach, California 90278, United States

[∥]Department of Chemical Engineering and [⊥]Department of Applied Physics and Applied Mathematics, Columbia University, New York, New York 10027, United States

Supporting Information

**ABSTRACT:** **The quest for the by-design assembly of material and devices from nanoscale inorganic components is well recognized. Conventional self-assembly is often limited in its ability to control material morphology and structure simultaneously. Here, we report a general method of assembling nanoparticles in a linear "pillar" morphology with regulated internal configurations. Our approach is inspired by supramolecular systems, where intermolecular stacking guides the assembly process to form diverse linear morphologies. Programmable stacking interactions were realized through incorporation of DNA coded recognition between the designed planar nanoparticle clusters. This resulted in the formation of multilayered pillar architectures with a well-defined internal nanoparticle organization. By controlling the number, position, size, and composition of the nanoparticles in each layer, a broad range of nanoparticle pillars were assembled and characterized in detail. In addition, we demonstrated the utility of this stacking assembly strategy for investigating plasmonic and electrical transport properties.**

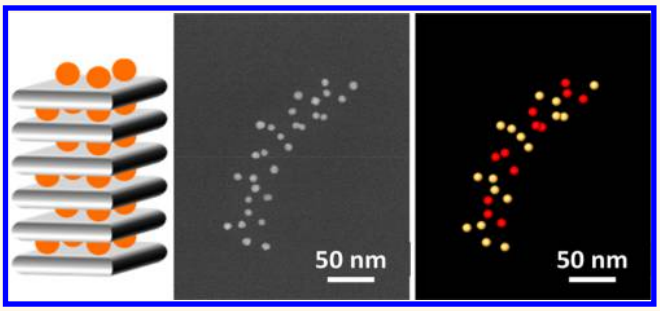


**KEYWORDS:** *DNA nanotechnology, DNA origami, nanoparticle, nanostructure, self-assembly, plasmonics*

Nanoparticles have been used as building blocks in material fabrication due to their specific optical, electrical, and magnetic functional properties. The assembly of nanoparticles into larger-scale structures not only integrates their intrinsic properties but also allows the exploration of cooperative and synergistic effects enabling material functionality in plasmonics,[1−3] photonics,[4] sensing,[5−7] catalysis,[5] and biomedicine.[8,9] Along this direction, varieties of assembly strategies have been developed to control the organization of nanoparticles by modulating their interactions, packing properties, and geometrical features.[7,10−12] These approaches have provided ample capabilities for affecting the phase behavior of assemblies, with ability to influence interparticle distances and lattice symmetry. However, the control over the morphology, an overall shape and texture of the assembled material, remains difficult, which is in part due to the limited abilities to guide the assembly process. In this respect, it is advantageous to establish the nanoscale fabrication strategies that mimic morphologically rich molecular synthesis and intermolecular assembly processes, which often occur in a sequential manner. For example, a recently demonstrated chain-like assembly of nanorods was inspired by a step-growth polymerization reaction,[13] and chain-like assembly of cubes was promoted by their edge−edge or face−face interaction.[14]

Supra-biomolecular assemblies provide a vivid illustration of structural complexity achieved through the combination of the molecule's architecture and the interactions of its different parts.[15,16] One of the broadly observed morphologies is the linear assembly of small biomolecules, which is commonly used by nature for a variety of biofunctions, including protein signaling and mechanical support and transport. Despite the linear character of this assembly, these structures exhibit a wide variety of architectures such as cylinders and tubes, flat and twisted ribbons, and others, depending on the molecular details. Here we explore adapting the supramolecular design

Received: April 17, 2017
Accepted: May 25, 2017
Published: May 25, 2017





DOI: 10.1021/acsnano.7b02671
ACS Nano XXXX, XXX, XXX−XXX

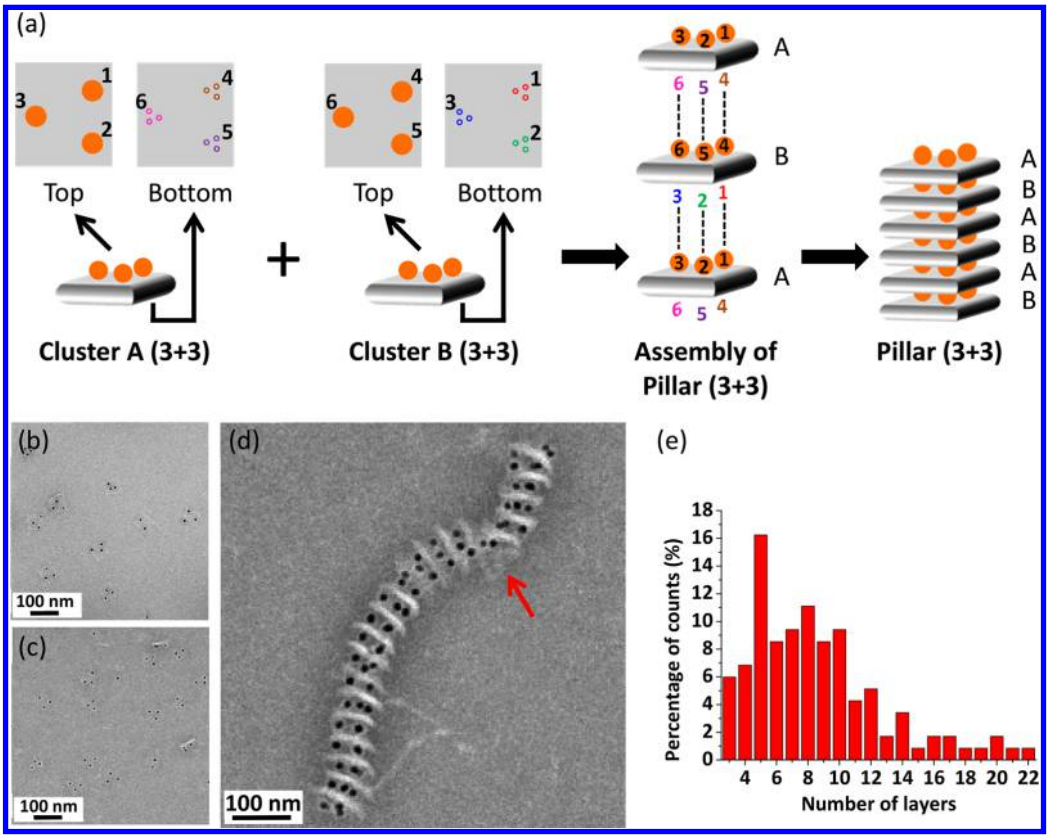


**Figure 1. Self-assembly of the supra-nanoparticle pillar, (3 + 3). (a) Assembly schematic of the pillar (3 + 3). Three gold nanoparticle binding sites are designed on the top and bottom of the DNA origami tile. Each binding site consists of three identical anchoring strands, which are labeled as circles with each color representing a unique DNA sequence. The clusters A and B are mixed and annealed to create a pillar (3 + 3). TEM images of the negative stained (b) cluster A (3 + 3), (c) cluster B (3 + 3), and (d) pillar (3 + 3). The red arrow points to the defect position, where two nanoparticles in one cluster are shared by three DNA tiles. (e) The histogram on the number of layers per pillar, obtained from 117 pillars (3 + 3).**

principles for assembly of nanomaterials in a desired linear configuration.

The formation of linear supramolecular assemblies typically originates from particular binding motifs, which then provides a double-sided and noncovalent association, *i.e.*, stacking. In this study, we exploit such a supramolecular strategy for building linear nanoparticle-based structures from planar nanoparticle-containing modules, interacting in a stacking manner. Moreover, the utilization of DNA hybridization as a noncovalent intermodular linker enables programming of these intermodular stacking interactions. Consequently, heteromodule linear architectures with complex internal organizations of nanoparticles can be assembled.

DNA directed self-assembly has been demonstrated as a powerful approach[17,18] to controlling particle linkages. More recently, those linkages were successfully translated into formation of three-dimensional (3D) superlattices of nanoparticles.[19,20] By controlling the size and shape of the nanoparticles, the length and sequence of the DNA linkers, and the topology of linking motifs, a wide range of 3D nanoparticle superlattices have been assembled.[19−27] In parallel, DNA templated assembly has been used for the formation of 1D and 2D assemblies of nanoparticles, including clusters,[28−37] linear structures,[34,38−41] helical structures,[42,43] and 2D arrays.[34,39,40,44−50] A broad variety of targeted DNA structures can be constructed, and even a deliberate assembly of point-to-point DNA linear structures was recently demonstrated,[51−55] however, it is difficult to achieve such level of control for nanoparticles. Therefore, a modular approach had been proposed for building complex particle organizations.[34,39,40,56] For example, for planar structures, nanoparticles are assembled into clusters, and then those clusters are further assembled into more complex superstructures using the prescribed DNA encoding.[39] In this study, we extend this idea to assembly of linear morphologies with 3D particle configurations. By combining programmable stacking interactions and the modularity of assembled planar nanoparticle clusters, we achieve supra-nanoparticle assembly of well-defined linear, pillar-like, morphology with a tailorable structure and composition. Detailed structural characterization using electron microscopy and X-ray scattering methods reveals that our assembled architectures are in a close correspondence with the designs, thus demonstrating the strength of this approach. Moreover, the modularity permits the assembly of both homo- and heteroparticle structures. The proposed assembly scheme, as we show, can be used for the control of optical responses of nanostructures and, potentially, in molecular electronics and energy transfer.

## RESULTS AND DISCUSSION

The proposed supra-nanoparticle assembly is a two-staged process: first, DNA-coated nanoparticles are assembled into a planar cluster scaffolded by a DNA origami tile, and then those clusters are assembled into the linear architectures we refer to as pillars (Figure 1). The assembly of these pillars is governed


DOI: 10.1021/acsnano.7b02671
ACS Nano XXXX, XXX, XXX−XXX

by DNA-programmable stacking in the direction normal of the planar nanoparticle clusters, with double-sided binding properties. In each planar cluster, the positions of nanoparticles are prescribed by the DNA origami tile. By controlling the configuration (number, position, and size) and composition of nanoparticles in each planar cluster, different modules can be created, and, correspondingly, nanoparticle pillars with variety of configurations can be assembled. The relative orientation of adjacent layers can be controlled by the position and sequence of DNA anchor strands extending from the DNA origami tile. As a result, we constructed a pillar (3 + 3) from stacking two types of 3-nanoparticle clusters, a pillar (3 + 4) made by alternating 3- and 4-nanoparticle clusters, a pillar (3 + 3)* stacked with different sizes of nanoparticles in the clusters, and a pillar (3 + 2) that stacks clusters with different nanoparticle compositions. In addition to demonstrating the versatility of this assembly process, we also investigated the impact of this assembly method on nanoparticle plasmonic and electrical transport properties.

**Homo-Particle Pillared Architectures.** In our approach, a double-layered DNA origami tile (~45 nm × 45 nm)[57] is employed as the template to immobilize gold nanoparticles at specifically designated positions. This double-layered DNA tile was reported to organize gold nanorods into helical structures.[57] In our study, we extend this approach for assembly of pillars with complex internal organization by enabling a control over number of particles per tile, particle encoding, particle site position, size of particles, and their composition. The double-layered tile provides more rigidity than a single-layered DNA origami, which is important for the robust assembly process and structural integrity of pillars.[57] On both sides of the tile, DNA anchor strands are designed in selected positions to provide anchor points for the nanoparticles. The DNA strands at each anchor point have their own unique DNA sequence coded for a nanoparticle hybridized with DNA strands having the complementary sequence.

In the case of the pillar (3 + 3), we start with three identical gold nanoparticles (9 nm Au core diameter) in an isosceles triangle configuration fixed on top of a DNA tile, to create the cluster A, as shown in Figure 1a. Each nanoparticle location on the top of the tile has its own DNA code, denoted as 1, 2, and 3. Corresponding DNA-coated gold nanoparticles can hybridize with matching codes 1, 2 and 3, thus, it results in their attachment to these locations. Likewise, on the bottom of the tile there are three symmetrical locations with their uniquely coded DNA unpaired anchor strands, denoted as 4, 5, and 6. To increase the nanoparticle binding yield to the tiles, three identical DNA anchor strands (circles with a same color, Figure 1a) for each code are designed in each anchor site to help capture a gold nanoparticle. To complete our building block set, a cluster B is created in order to alternately stack with the cluster A. As shown in Figure 1a, for the cluster B, the gold nanoparticles are fixed on the top of the tile with DNA codes 4, 5, and 6, while the unpaired DNA anchor strands on the opposite side are coded 1, 2, and 3, respectively. Once the clusters A and B have been fabricated, they are then mixed together, and the layers self-assemble into the desired ABAB sequence to form a nanoparticle pillar. The reason for the A−B layer approach is that if just one A layer was used with identical 1, 2, and 3 codes on the top and bottom, one flipped tile might bind to the other nonflipped tile *via* two of the three binding sites. Therefore, if only one kind of layer was used, individual layers might bind to each other at the wrong points resulting in misalignments and an uncontrolled stacked structure.

The formation of the individual clusters was first investigated by transmission electron microscopy (TEM). To increase the contrast of the DNA origami, the samples were stained by uranyl acetate. The TEM images (Figures 1b, c, and S1and S2) show that most of layers were flat and contained three gold nanoparticles as designed. The gold nanoparticles showed slightly different separations in the clusters, as a result of certain flexibility in the DNA linkers and the capillary forces during the drying process inherent in the TEM sample preparation,[58] and in rare cases the clusters exhibited folding. In some clusters, only one or two nanoparticles were visible, which is due to the partial or complete overlap of the nanoparticles and/or the defect of the assembly of individual clusters. Statistical analysis based on the TEM images indicated that the assembly yield without any purification step of the cluster A (3 + 3) and cluster B (3 + 3) were quite high, 83.8% and 81.2%, respectively.

Figure 1d shows a TEM image of the pillar (3 + 3) in which nanoparticle layers are stacked up to form a linear structure with a submicron dimension. Based on the TEM images, the interlayer distances was measured to be 24.2 ± 3.2 nm, which is in the designed range of 23.4−30.2 nm considering the flexibility of the DNA single strands. We attribute the curvature observed in these structures to the flexibility of the anchor and nanoparticle grafted strands and to random defects in the assembly and TEM sample preparation. For example, in Figure 1d, two nanoparticles in one cluster (pointed by the red arrow) were shared by three DNA tiles which led to the defect in a linear morphology. However, this defect did not break the structure. Since each cluster has multiple nanoparticle binding sites, even if only one of the binding sites captures the nanoparticle, this cluster can still link with other clusters to form a longer, pillared structure, which reveals the error-forgiving properties of this assembly scheme. Such redundancy in the design can be useful for optical and electric functions, where missing a single particle for a chain-like arrangement could ruin energy or charge transfer. Low-magnification TEM images show that pillars with diverse lengths were observed (Figures S3g−i), with some of the structures cross-linked through one shared nanoparticle. The statistical analysis of the length of the pillars indicates that the majority are 5−10 layers long (Figure 1e). Although the error-forgiving scheme tolerates defects in the assembly, the length of these pillars is limited mainly by the initial concentration of the individual clusters[57] and their precipitation of the assemblies.

To reveal the native 3D structure of the pillar and to verify its correspondence with conventional TEM imaging and related sample preparation, we have performed cryogenic scanning transmission electron tomography (CSTET) on selected samples for 3D structural visualization. The pillar (3 + 3) structures were first frozen in their native state and then were imaged using annular dark-field scanning transmission electron microscopy (ADF-STEM) (Figures 2 and S4 and S5). Figure 2 shows the comparison of the CSTET projection images (Figure 2 top) at different tilt angles and the corresponding reconstructed models (Figure 2 bottom). The position of the nanoparticles matches well with that in the model at different tilt angles. The color labeled reconstructed model clearly indicates the triangular orientation of nanoparticles in each layer, expected for the triangular position of anchoring spots on the DNA tile, and the relative orientation of cluster layers. The


DOI: 10.1021/acsnano.7b02671
ACS Nano XXXX, XXX, XXX−XXX

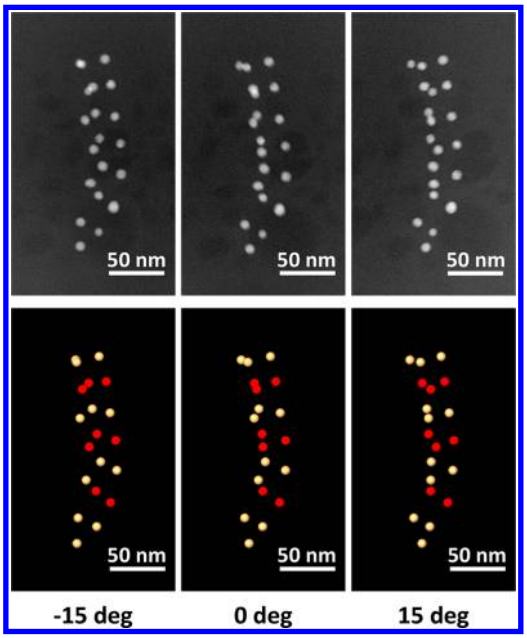


**Figure 2. CSTET images (top) and the corresponding reconstructed model (bottom) of the pillar (3 + 3) at different tilt angles. Nanoparticles fixed in two different clusters are labeled as red and yellow in the reconstructed model, respectively. Additional CSTET images and corresponding videos of reconstructed models are included in the Supporting Information and Movie S1 and S2.**

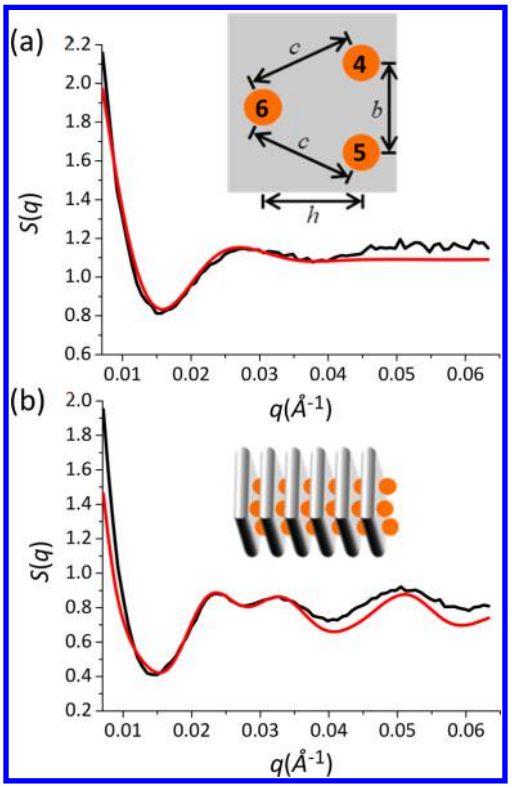


**Figure 3. SAXS measured structure factor $S(q)$ (black) and the associated modeling fit (red) of (a) the cluster B (3 + 3) and the pillar (3 + 3). The scheme of the center-to-center distance of nanoparticles of the cluster A (3 + 3) and cluster B (3 + 3) is shown in the inset of (a), and the scheme of the pillar (3 + 3) is shown in the inset of (b).**

interlayer distance measured in the reconstructed model was 28.8 ± 4.0 nm, in agreement with the designed range. The somewhat smaller spacing observed by negatively staining TEM sample is attributed to dehydration during the drying and staining process. The reconstructed model yields interparticle distances 20.9 ± 1.6, 23.8 ± 2.2, and 25.9 ± 2.1 nm. According to the original design of the tiles, the center-to-center distance between nanoparticles in positions 1 and 2 (or 4 and 5) was expected to be between 20.0 and 25.0 nm, assuming the distance between adjacent duplexes is 2.0 and 2.5 nm. The center-to-center distance between nanoparticles in positions 1 and 3 (or 4 and 6), and positions 2 and 3 (or 5 and 6), was expected to be between 23.0 and 24.2 nm, assuming the pitch of the duplex is 3.4 nm. Thus, the measured distances are close to the expected values. It needs to be noted that the overall pillar structure and its internal organization in solution are dynamic due to the flexibility of single-strand DNA linkers, so the reconstructed model only records one specific stage of the structure and cannot represent the average configurations. Certain deviation from expected values due to the cryo-sample preparation is also possible. Overall, the negative stained TEM images and reconstructed models show a consistent pillared structure, and both agree with the system design.

In addition to TEM, small-angle X-ray scattering (SAXS) was employed for an in-solution investigation of the ensemble averaged structure of the individual clusters and the stacked pillars. The SAXS measured structure factor and the associated modeling fit confirmed the formation of the individual cluster in solution and revealed the distances between nanoparticles (Figure 3a and Supporting Information and Table S1). As mentioned above, the center-to-center distance, $b$, between nanoparticles in positions 1 and 2 (or 4 and 5) was expected to be between 20.0 and 25.0 nm, and the center-to-center distance, $c$, between nanoparticles in positions 1 and 3 (or 4 and 6), and positions 2 and 3 (or 5 and 6), was expected to be between 23.0 and 24.2 nm. For convenient comparison between different pillar designs, we introduce the parameter $h$, which is a distance between position 3 and a line connecting positions 1 or 2 (or between position 6 and a line connecting positions 4 or 5) and was designed to be 20.7 nm (Figure 3a). The SAXS modeling fit showed that the distances $b$ and $c$ were 23.5 and 29.0 nm, respectively (Table S1). According to the value of $b$ and $c$, the distance $h$ was obtained as 26.5 nm. The distance $b$ is in the expected range, while $c$ and $h$ are both somewhat larger than anticipated by the design. That discrepancy might be attributed to flexibility of single-stranded DNA linkers which might stretch and tilt due to the electrostatic repulsion between particles. The length of the fully extended DNA linker is 10.6 nm assuming the length per single strand DNA base is 0.676 nm. Once the DNA linker in the binding site 6 tilts toward the edge from the normal direction by 35°, the distance $c$ would be in the range of 28.4−29.7 nm, and $h$ would be 26.8 nm. In this case the measured distances $c$ and $h$ would be in the expected range. Besides, not only for binding site 6 but also in the binding sites 4 and 5, the DNA linkers would stretch and tilt, so an even smaller tilt angle would result in a significant increase of $c$.

The structure of solution dispersed assembled pillars (3 + 3), was probed by SAXS (Figure 3b) and was quantitatively modeled by stacking of clusters (see Supporting Information). The SAXS measured structure factor, $S(q)$, and the modeling fits of the pillar (3 + 3) confirmed the stacking arrangements of the nanoparticle clusters. Although the best match with the



DOI: 10.1021/acsnano.7b02671
ACS Nano XXXX, XXX, XXX−XXX

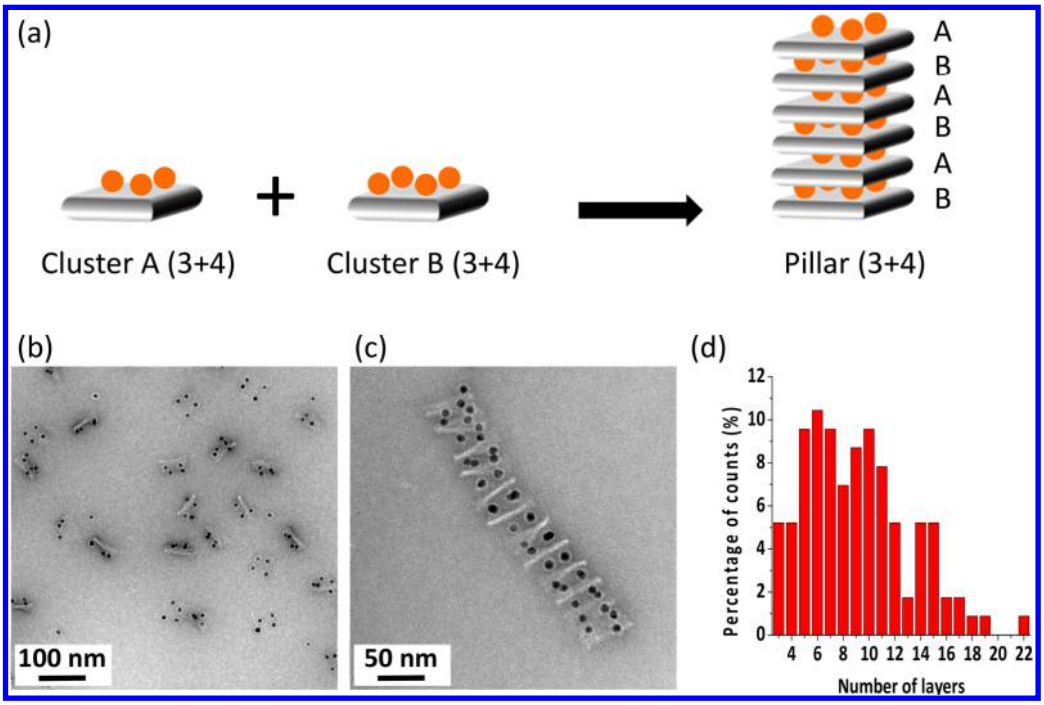


**Figure 4. Self-assembly of the pillar (3 + 4). (a) The scheme of the assembly of the pillar (3 + 4). TEM images of the negative stained (b) cluster B (3 + 4) and (c) pillar (3 + 4). (d) The histogram of observed multilayered pillars, obtained from 115 pillars (3 + 4).**

SAXS data is observed for a three-layered pillar model, our analysis indicates that scattering features are quite similar for pillars with 3−5 layers (Figure S20), which is expected for a periodic structure. We note that the bending and loss of correlation between layers within the pillar can contribute to the lower detected number of layers in comparison to TEM. The SAXS analysis yields the interlayer distance of 28.2 nm that is in the designed range of 23.4−30.2 nm and close to the interlayer distance measured from the 3D reconstructed models (28.8 ± 4.0 nm). Thus, the solution SAXS measurements confirm that assembly of the pillar structure occurs in the solution, and the observed structure agrees well with the CSTET imaging and the design.

**Heterostructured Pillars.** One of the strengths of our assembly strategy is that the internal organization of the pillars including the number, position, size, and composition of nanoparticles in each layer can be rationally controlled. To demonstrate the versatility of our method, we have designed a system with different numbers and positions of the nanoparticles on each of the two AB clusters to create the pillar (3 + 4) (Figure 4a). In this case, a new cluster A (3 + 4) is constructed, which has the same three gold nanoparticles on the top of the tile, but has four DNA coded anchor points fixed to the bottom of the tile. Likewise, another new cluster B (3 + 4) was constructed that has four gold nanoparticles fixed to the top of the tile, but with three DNA anchors sitting on the bottom. The TEM image shows that most of the cluster B had four nanoparticles with a yield of 66.4% (Figures 4b and S7). The lower assembly yield is because 20.1% of cluster B contained five nanoparticles, which results from the partial hybridization of the nanoparticles to the anchor strands at the bottom. This partial hybridization, however, was not stable and would be broken during the following assembly of the stacked structure and replaced by the complete hybridization with the target nanoparticle. The clusters A and B were then mixed and annealed to assemble the pillar (3 + 4). As expected, the TEM images show that the cluster A (3 + 4) and cluster B (3 + 4) stacked alternatively to form a linear, stacked structure (Figures 4c and S8). The TEM measured interlayer distance is 21.1 ± 1.7 nm, which is smaller than expected from the design. The effects of dehydration and staining required for the sample preparation can contribute to that. The pillar length distribution, as obtained from the TEM images, indicates that the pillars are mainly 5−11 layers long, which is similar to the length observed in the TEM images of the pillar (3 + 3) (Figure 4d).

The pillar (3 + 4) was also characterized by CSTET (Figures 5 and S9 and S10). The electron microscopy images matched with the reconstructed model very well. The interlayer distance was measured to be 26.9 ± 1.6 nm, which is in the designed range of 23.4−30.2 nm and larger than the value measured from the negative stained TEM images. We also found the interparticle distances in both cluster A (3 + 4) and cluster B (3 + 4) based on the 3D reconstruction model. The interparticle distances in the cluster A (3 + 4) were 24.6 ± 2.3, 24.9 ± 5.3, and 26.5 ± 2.1 nm, which are either in or close to the designed range. Compared with the value obtained from the reconstructed model of the pillar (3 + 3), the interparticle distances were slightly larger. As we noted above, the interparticle distance measured from the 3D reconstruction model can only represent a specific stage of the structure, so we attribute the difference to the flexibility of the DNA linkers and dynamic motion of the pillar. The measured interparticle distances in the cluster B (3 + 4) were 23.0 ± 4.8, 23.3 ± 5.3, 26.0 ± 4.4, and 28.9 ± 2.4 nm. We assigned the smaller two values to the distance *b* and the larger two values to the distance *a*. The measured distance *b* is consistent with the design, while *a* is a bit larger than the expected value, likely due to the flexibility of the DNA linkers. The CSTET images and reconstructed models further confirm the formation of the planar particle cluster and the consequent stacking assembly of


DOI: 10.1021/acsnano.7b02671
ACS Nano XXXX, XXX, XXX−XXX

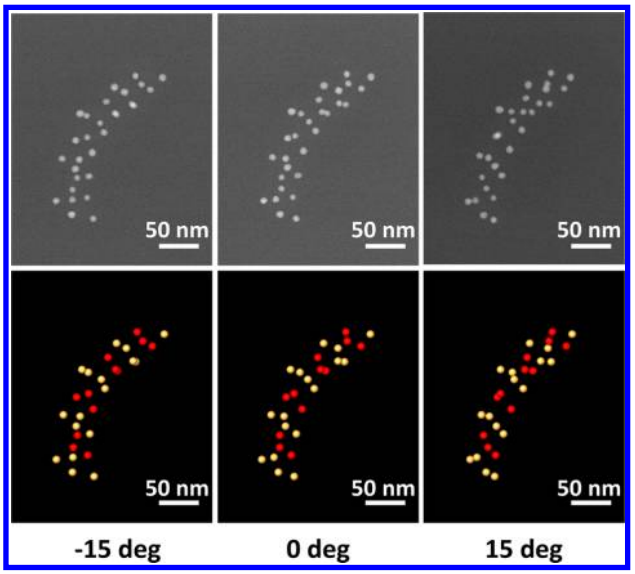


**Figure 5. CSTET image (top) and the corresponding reconstructed model (bottom) of the pillar (3 + 4) at different tilt angles. In the reconstructed model, nanoparticles in the cluster A (3 + 4) are labeled as red, and nanoparticles in the cluster B (3 + 4) are labeled as yellow. Additional CSTET images and corresponding videos of reconstructed models are in the Supporting Information and Movies S3 and S4.**

different clusters into pillars, which is consistent with our design.

In addition to the direct imaging by electron microscopy, the ensemble structures of the cluster B (3 + 4) and the pillar (3 + 4) were investigated by the solution SAXS. Figure 6a shows the structure factor and the modeling fit of the cluster B (3 + 4). According to the design, the distances *a* and *b* are expected to be 25.9 nm and 20.0−25.0 nm, respectively. The fitting result indicated that the measured distances *a* and *b* were close to the expected values, correspondingly, 26.0 and 23.5 nm (Table S1). The designed distance *a* in the cluster B (3 + 4) is larger than the designed distance *h* in the cluster B (3 + 3), which led to weaker electrostatic repulsion (Table S1). The structure factor, $S(q)$, of the pillar (3 + 4) and the modeling fits confirmed the stacking arrangement of the clusters with an interlayer distance of 27.5 nm, close to the interlayer distance of the pillar (3 + 3) and the result measured from the 3D reconstruction models. The fit yields a four-layered pillar; however, as we discussed for the (3 + 3) case, SAXS measurements are not sensitive to identify the exact number of layers (Figures 6b and S21). The SAXS confirms in-solution assembly of the pillars (3 + 4), and it provides *in situ* information on interparticle and interlayer distances, which complement TEM and CSTET imaging from the corresponding stained and cryo-prepared samples.

**Pillars with Varying Nanoparticle Sizes.** In addition to the number and position of the nanoparticles, the size of the nanoparticles can be also controlled in this assembly process. In this design, we increased the diameter of spherical gold nanoparticles in the cluster A (3 + 3) from 9 to 15 nm, resulting in a cluster A (3 + 3)* (Figure 7a). The cluster B (3 + 3)* is same as the original cluster B (3 + 3). The TEM image indicates that the cluster A (3 + 3)* was successfully assembled with a yield of 82.6% (Figures 7b and S11). The relative orientation of three nanoparticles is same as that of the cluster A (3 + 3). The formation of the pillar (3 + 3)* was confirmed by TEM, which clearly shows that layers of 15 and 9 nm

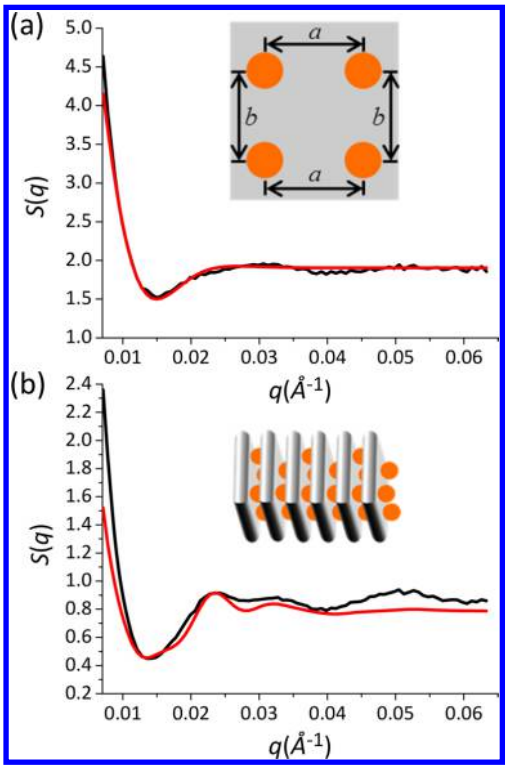


**Figure 6. SAXS measured structure factor $S(q)$ (black) and the associated modeling fit (red) of (a) the cluster B (3 + 4) and the pillar (3 + 4). The scheme of the center-to-center distance of nanoparticles of the cluster B (3 + 4) is shown in the inset of (a), and the scheme of the pillar (3 + 4) is shown in the inset of (b).**

nanoparticles alternatively stacked to form a linear structure (Figures 7c,d and S12a−f). It was observed that some layers contained only two nanoparticles, leading to a curvature of the linear structure. Four nanoparticles also could be found in some layers, which is because one free nanoparticle in the solution first bound to the bottom side of one of the clusters. Thus, only two free binding sites were left for the other cluster, resulting in four nanoparticles in that layer. The interlayer distance was measured to be 24.4 ± 2.9 nm, which is in the designed range and similar to that of the pillar (3 + 3). The histogram of TEM observed pillar shows that the majority of the assembled pillars have 5−8 layers, which is slightly shorter than the pillar (3 + 3). As the size of the nanoparticle increases, the number and density of DNA strands on the nanoparticles increase, which further promotes the repulsion between the DNA origami tile and nanoparticles.

**Plasmonic Properties of Assembled Pillars.** These assembled pillars provide a useful platform to investigate the plasmonic effects in linear assemblies, which were considered for energy transfer. The collective plasmon resonance highly depends on the interparticle spacing, the geometry of the nanoparticles and their arrangements. The manipulation of the plasmon resonance enables a broad range of applications including metamaterials, sensing, and optical waveguides.[1−3] To tune the plasmon resonance of the designed system in our study, the size of nanoparticles and the interparticle spacings were changed by the electroless deposition of gold from a solution onto gold nanoparticles already present in the assembled pillars. The stacked structure not only allows the plasmonic coupling within each layer but also enables plasmonic coupling between adjacent layers. As the number


DOI: 10.1021/acsnano.7b02671
ACS Nano XXXX, XXX, XXX−XXX

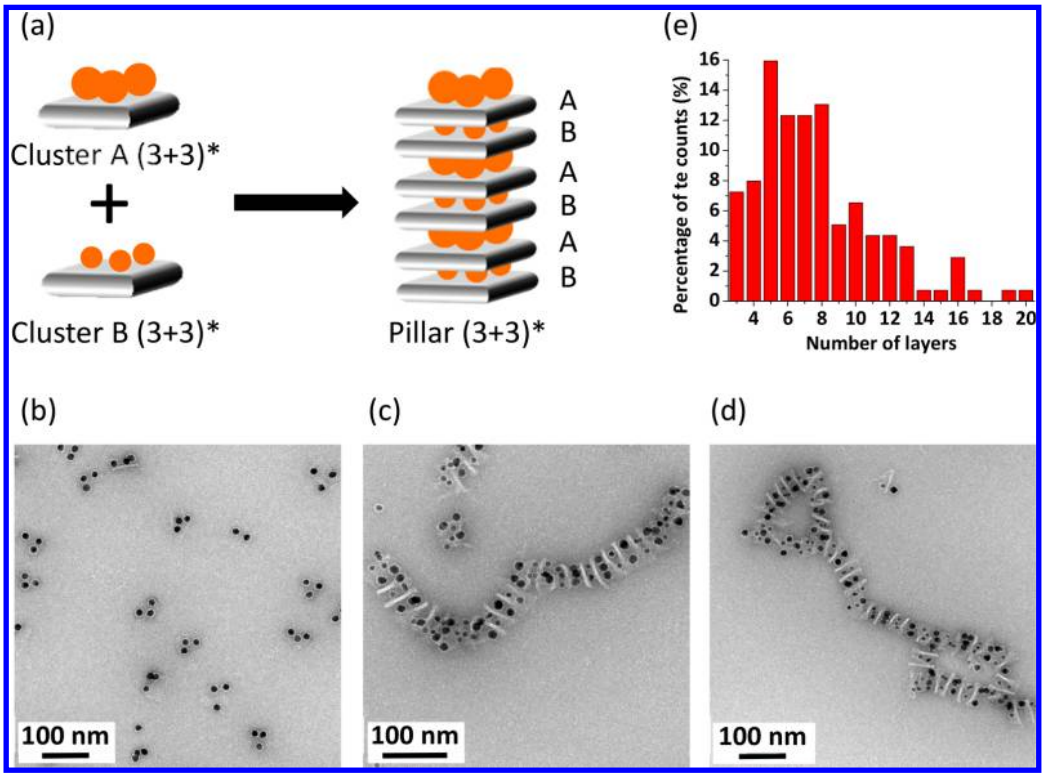


Figure 7. Self-assembly of the pillar (3 + 3)*. (a) The scheme of the assembly of the pillar (3 + 3)*. TEM images of the negative stained (b) cluster A (3 + 3)* and (c, d) pillar (3 + 3)*. (e) The histogram of pillars, as obtained from 138 pillars (3 + 3)*.

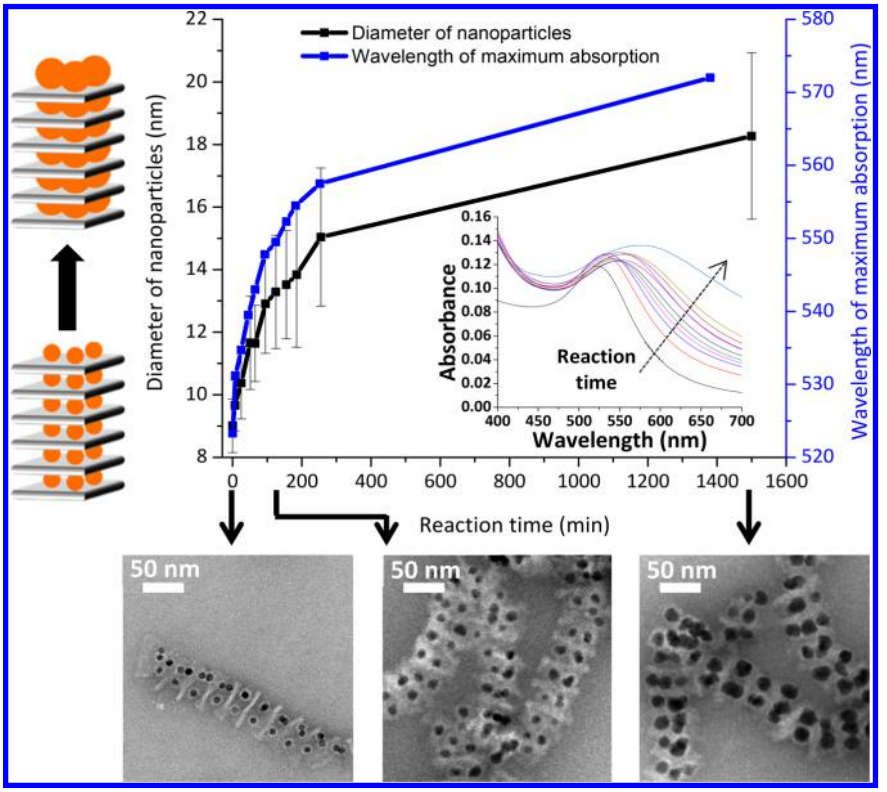


Figure 8. Tuning of the surface plasmon resonance by metal deposition within an existing nanostructure. The averaged diameter of gold nanoparticles and the wavelength of maximum absorption during nanoparticle growth are shown. The TEM images at 0, 125, and 1500 min growth reaction are shown at the bottom. Inset shows the UV−vis absorption spectra of the pillar (3 + 3) during the growth of the gold nanoparticles. The dashed arrow indicates the direction of the shift of the curve as the growth reaction time increases. The UV−vis absorption spectra with the label of each curve are shown in Figure S13.



DOI: 10.1021/acsnano.7b02671
ACS Nano XXXX, XXX, XXX−XXX

of layers increases, the layer-to-layer coupled plasmonic redshift dominates the redshift from the nanoparticle coupling within the layer. Figure 8 shows that as the electroless deposition reaction time increases, the size of gold nanoparticles in the pillar increased from 9.0 to 18.3 nm in 1500 min, and the rate of the growth gradually decreased. TEM images of the pillar (3 + 3) at different reaction times show that such modifications did not affect the pillared structure or internal nanoparticle organization. However, some nanoparticles did not maintain their spherical shape during the growth, and aggregations of pillars were observed. To characterize the impact on plasmon resonance, the corresponding UV−vis absorption spectra were collected. Before the gold deposition, the resonance wavelength of the pillar (3 + 3) was 523 nm. As the reaction time increases, the resonance wavelength red-shifted and the peak broadened. After 1380 min of reaction, the resonance wavelength shifted to 572 nm.

We have conducted the finite-difference time-domain (FDTD) numerical simulation of the plasmon resonance for our architecture to reveal the origin of the observed redshift (see Supporting Information). The FDTD analysis indicates that the resonance wavelength is expected to redshift by *ca.* 24 nm when the size of particles increased from 9.0 to 18.0 nm (Figure S22). However, the UV−vis absorption spectra show that the resonance wavelength shifted from 523 to 572 nm, which is almost double the theoretical shift. The extra redshift may result from the change of the shape of nanoparticles, aggregation of nanoparticles in the solution, and growth of free particles. As mentioned above, TEM images indicate that during the gold enhancement, some of the gold nanoparticles did not maintain their spherical shape, which would contribute to the redshift of the resonance wavelength (Figure 8). Besides, the aggregation of nanoparticles might be generated by some free nanoparticles and/or nanoparticles that were seeded and grown from the gold enhancement reagent during the gold deposition process. Figure S13 shows that as the reaction time increased, the surface plasmon resonance peaks broadened, which further confirms the formation of the aggregation. Such aggregation would significantly contribute to the redshift of the resonance wavelength.

**Electrical Transport of Assembled Pillars.** The electrical transport property of the nanoparticle pillar, due to its linear character, is of interest for potential charge-transfer applications. To measure electrical transport, the pillar (3 + 3) was deposited and dried on a $SiO_2$/Si wafer with patterned gold pads. Regions of high density of the pillars were identified by a scanning electron microscope (SEM) incorporated in a dualbeam focused ion beam (FIB) system (Figure 9a). Due to the low conductivity of the DNA, the DNA tiles and linker strands could not be observed, and only the gold nanoparticles appear in the images. The 800 nm-thick isolation $SiO_2$ layer also led to charging problems during the SEM imaging; therefore no higher magnification images were obtained. To connect the pillars to the gold pads, two platinum electrodes were generated by FIB-induced deposition to connect the pads *in situ* to the pillars (Figure 9b). In this process, low current and accelerating voltage had to be used in order to minimize the damage of the structure.[59] To avoid the possible effect of platinum scattered from the designated electrodes into the interval between two electrodes, the distance between the deposited platinum electrodes was kept at *ca.* 500 nm. A current−voltage ($I$−$V$) curve for the pillar was recorded over the range from −10 to 10 V (Figure 9c), showing a clear

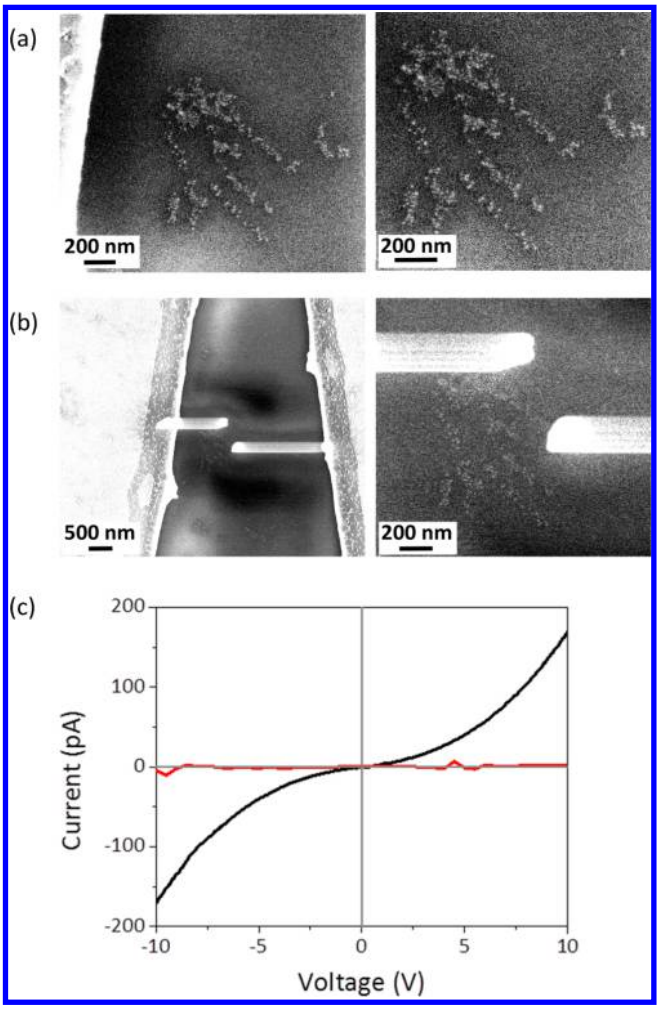


**Figure 9. Electrical transport of the pillar (3 + 3). SEM images of the pillar (3 + 3) deposited on a $SiO_2$/Si wafer with patterned gold pads (a) before the deposition of the platinum electrodes and (b) after the deposition of the platinum electrodes. The zoomed-in images are shown on the right. (c) Current−voltage ($I$−$V$) measurement of the sample in (b) (black) and the control sample shown in Figure S14 where there is no pillar between two electrodes (red).**

power-law behavior, $I \propto V^3$. To eliminate the effect of the buffer, substrate, and the platinum electrodes, we conducted a control experiment where no pillar could be found between two platinum electrodes (Figure S14a). The associated $I$−$V$ curve was identical to the instrument noise in the working environment and indicated an electric cut off, which demonstrated that the power-law behavior resulted from the nanoparticle pillar (Figures 9c and S14b). A similar power-law behavior, observed in carbon nanotubes,[60,61] polymer nanofibers,[62] and polymer/DNA nanonecklaced structures,[63] is generally interpreted as indicative of tunneling of charge carriers in 1D systems. However, a variable range hopping mechanism was also proposed to explain the power-law behavior in polymer nanofibers.[64] A complete understanding of the transport mechanism in our system requires additional investigations, in particular $I$−$V$ measurements at different temperatures.

**Pillars with Variable Nanoparticle Composition.** Our cluster stacking approach can also be applied for fabrication of nanoparticle pillar architectures with complex heterogeneous


DOI: 10.1021/acsnano.7b02671
ACS Nano XXXX, XXX, XXX−XXX

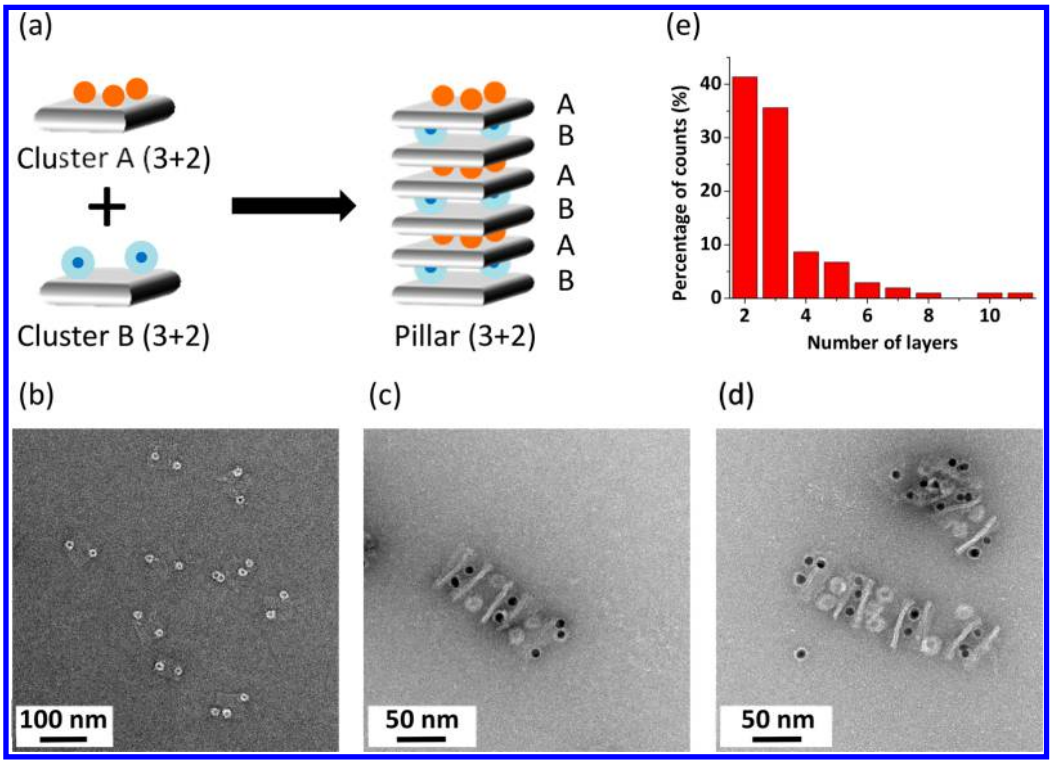


**Figure 10. Self-assembly of the heterocomposed pillar (3 + 2) from gold nanoparticles and QDs. (a) The scheme of the assembly of the pillar (3 + 2). TEM images of the negative stained (b) cluster B (3 + 2) and (c, d) pillar (3 + 2). (e) The histogram of formed pillars, obtained from 104 pillars (3 + 2).**

composition. Figure 10a shows the design of a pillar (3 + 2) in which layers of gold nanoparticles and layers of quantum dots (QDs) are alternatively stacked. The QDs are composed of a cadmium selenide core with a zinc sulfide shell and exhibit an emission maximum at 605 nm. For this structure, a new cluster A (3 + 2) is constructed, with three gold nanoparticles (9 nm in diameter) on the top of the DNA tile, but with only two DNA anchor locations on the bottom of the tile. Likewise, a new cluster B (3 + 2) has two QDs fixed on the top side, and three DNA anchor points on the bottom of the tile. Each QD is coated with streptavidin leading to a QD diameter of 15−20 nm. To anchor the QD on the DNA origami tile, the dual-biotin groups were modified at the end of the anchor strands on the bottom side of the cluster A (3 + 2) and the top side of the cluster B (3 + 2). The QD-streptavidin conjugates are anchored through the biotin−streptavidin interaction. We first investigated the binding behavior of the DNA origami tile-QD conjugates. Figures 10b and S16 show that 46.2% of the cluster B (3 + 2) has two QDs, and three QDs were observed in 27.2% of the clusters. Since each binding site has three anchor strands, as discussed above, and each anchor strands contains two biotin groups, it is possible that these six biotin groups bind to two QDs at the same time. Also, unlike the anchoring of gold nanoparticles, the QDs were captured by the biotin−streptavidin interaction instead of the DNA hybridization. Thus, during the annealing, the anchoring of the QD could not be reorganized to minimize the energy, resulting in multiple QDs in a single binding site. Reducing the number and length of the binding strands could potentially solve this problem, but it might also lead to a lower binding efficiency.[58]

The assembled structure of the pillar (3 + 2), characterized by TEM, consists of alternating layers of gold nanoparticles and QDs, as expected (Figures 10c,d and S17). The interlayer distance was 29.0 ± 1.8 nm, which is in agreement with design. However, most of the pillars only have 2−3 layers (Figure 10e). It has been reported that the dissociation constant of the biotinylated DNA origami and streptavidin-modified QD complex is much higher than that of the free biotin-streptavidin complex.[58] Thus, the low binding efficiency between the cluster A (3 + 2) and cluster B (3 + 2) might hamper their assembly. Besides, in contrast to biotin−streptavidin interaction, the cycled annealing process for the gold-only pillars facilitates the assembly of the longer linear structures. Although the pillar (3 + 2) has a small number of layers, this result demonstrates the capability of organizing nanoparticles with diverse compositions into pillar structures. Such systems might provide a platform to study energy-transfer phenomena in the future studies.

## CONCLUSIONS

Inspired by suprabiomolecular assembly governed by stacking interactions, we have developed a versatile strategy to assemble nanoparticles of diverse sizes and compositions into nanoparticle pillars with tailorable internal nanoparticle configurations. The number, position, size, and composition of the nanoparticles can be rationally regulated in this process. These assembled pillars have been used to study the collective plasmon resonance for metal nanostructures, and the measured electrical transport properties of these pillared metal nanostructures may enable their application in molecular electronics. The developed assembly approach offers a general method of creating layered, pillared heterostructures with controllable linear morphology and nanoparticle configurations, and it may be used potentially for creation of future nanoparticle-based functional materials.



DOI: 10.1021/acsnano.7b02671
ACS Nano XXXX, XXX, XXX−XXX

## MATERIALS AND METHODS

**Self-Assembly, Purification, And Quantification of the Double-Layered DNA Origami Tile.** The single-stranded M13mp18 DNA genome was purchased from Bayou Biolabs. All unmodified staple strands were purchased from Integrated DNA Technologies, Inc. and used without additional purification. All anchoring strands, purchased from Integrated DNA Technologies, Inc., were purified with the polyacrylamide gel electrophoresis (PAGE) by the manufacturer. The double-layered DNA origami tile was designed using cadnano software (http://cadnano.org). The DNA origami tile was synthesized by mixing the single-stranded M13mp18 DNA genome, unmodified staple strands, and anchoring strands with a ratio of 1:20:20 in TAE/$Mg^{2+}$ buffer [tris (40 mM, pH 8.0), acetic acid (20 mM), EDTA (1 mM), and Mg $(CH_3COO)_2$ (12.5 mM)]. The final concentration of M13mp18 DNA genome is 5 nM. The solution was slowly cooled down from 90 to 80 °C over 9 min, from 80 to 70 °C over 100 min, and from 70 to 25 °C over 18 h in a Eppendorf Mastercycler. After the annealing, 200 μL of DNA origami solution was purified by rinsing away excess staple strands using TAE/$Mg^{2+}$ buffer in a 100 kDa MW centrifuge filter (EMD Millipore) on a centrifuge (Eppendorf) with a speed of 400×*g* at 20 °C. The rinsing process was repeated for another four times, and a total of 2100 μL of TAE/$Mg^{2+}$ buffer was used. The final volume of DNA origami solution was *ca.* 80 μL. The purified DNA origami tile was quantified by measuring the absorbance at 260 nm on a LAMBDA 35 UV−vis spectrophotometer (PerkinElmer).

**Preparation and Quantification of the DNA-Gold Nanoparticle Conjugates.** The thiolated DNA strands, purchased from Integrated DNA Technologies, Inc., were purified with high-performance liquid chromatography (HPLC) by the manufacturer. The disulfide bond on the thiolated DNA strand was first reduced by mixing thiolated DNA strands with the tris(2-carboxyethyl)phosphine (TCEP) solution (Sigma-Aldrich) with a ratio of 1:100 in water at 20 °C. After 2 h of incubation, the thiolated DNA strand was purified by the MicroSpin G-25 columns (GE Healthcare). Then the purified thiolated DNA strands were mixed with aqueous spherical gold nanoparticle solution (Ted Pella) with a ratio of 300:1 for 9 nm gold nanoparticles and 800:1 for 15 nm gold nanoparticles. After 2 h of incubation, the 10× phosphate-buffered saline (PBS) (100 mM, pH 7.4) was added to bring the final solution to be 1 × PBS (10 mM, pH 7.4). After another 2 h of incubation, the stepwise addition of the PBS buffer with 2 M sodium chloride increased the concentration of the sodium chloride to 0.3 M. The solution was allowed to age for 12 h. To remove the excess thiolated DNA strands, the solution was centrifuged, resulting in the precipitation of DNA-gold nanoparticle conjugates at the bottom of the tube. Then the supernatant was removed, and the fresh PBS buffer with 100 mM sodium chloride was used to rinse and finally dissolve the DNA-gold nanoparticle conjugates. The DNA-gold nanoparticle conjugates were quantified by measuring the absorbance at 520 nm on a LAMBDA 25 UV−vis spectrophotometer (PerkinElmer).

**Self-Assembly, Purification, and Quantification of the DNA Origami-Gold Nanoparticles Clusters.** The as-synthesized DNA origami tile was mixed with the DNA-gold nanoparticle conjugates with a ratio of 1:3 in TAE/$Mg^{2+}$ buffer. The solution was heated at 50 °C for 20 min and then slowly cooled down from 50 to 20 °C over 20 h. To remove the excess gold nanoparticles, the sample was purified by 0.75% (DNA origami-15 nm gold nanoparticles cluster) or 1% (DNA origami-9 nm gold nanoparticles cluster) agarose gel in a 0.5 × TBE buffer [tris (89 mM, pH 8.0), EDTA (2 mM), and boric acid (89 mM)] with 10.5 mM magnesium chloride at 20 °C. After the gel electrophoresis, the band of the DNA origami-gold nanoparticle clusters was cut and chopped into small pieces using a clean razor blade. The sample was extracted from the gel pieces using a Freeze 'N Squeeze DNA Gel Extraction Spin Column (Bio-Rad). The purified DNA origami-gold nanoparticles clusters were quantified by measuring the absorbance at 520 nm on a LAMBDA 25 UV−vis spectrophotometer (PerkinElmer).

**Self-Assembly, Purification, and Quantification of the DNA Origami-Quantum Dot Clusters.** The as-synthesized DNA origami tile was mixed with the quantum dot-streptavidin conjugates (Qdot 605, Invitrogen) with a ratio of 1:5 in TAE/$Mg^{2+}$ buffer. The solution was incubated at room temperature over 16 h. To remove the excess QDs, the sample was purified by 0.75% agarose gel in a 0.5 × TBE buffer with 10.5 mM magnesium chloride at 20 °C. After the gel electrophoresis, the band of the DNA origami-quantum dot clusters was cut and chopped into small pieces using a clean razor blade. The sample was extracted by the gel pieces using a Freeze 'N Squeeze DNA Gel Extraction Spin Column (Bio-Rad). The purified DNA origami-quantum dot clusters were quantified by measuring the fluorescence emission at 605 nm with 350 nm excitation on a Cary Eclipse fluorescence spectrophotometer (Varian).

**Self-Assembly of the Nanoparticle Pillar.** The purified cluster A and the corresponding cluster B were mixed with a ratio of 1:1 in TAE/$Mg^{2+}$ buffer. The solution was heated to 45 °C and slowly cooled down to 35 °C over 12 h. The annealing process was repeated for another three times. At the end of the last annealing cycle, the solution was slowly cooled to 20 °C.

**Gold Enhancement on the Assembled Pillars.** The GoldEnhancement kit was purchased from Nanoprobes (cat. no. 2114). The as-synthesized pillar was mixed with the GoldEnhancement reagent with a volume ratio of 1:0.3.

**UV−vis Spectrophotometer Measurement.** The DNA origami was quantified by measuring the absorbance at 260 nm on a LAMBDA 35 UV−vis spectrophotometer (PerkinElmer). The DNA-gold nanoparticle conjugates and DNA origami-gold nanoparticle clusters were quantified by measuring the absorbance at 520 nm on the LAMBDA 25 UV−vis spectrophotometer (PerkinElmer). The UV−vis spectra of the pillar during the gold enhancement were measured on the LAMBDA 25 UV−vis spectrophotometer (PerkinElmer).

**TEM Imaging of the Negative Stained Sample.** The carbon-coated grid (300 mesh, Ted Pella, product no. 01843-F) was first glow discharged using a PELCO easiGlow glow discharge cleaning system (Ted Pella). Then a drop of 5 μL of the sample solution was deposited on the carbon-coated grid and incubated for 5 min. Excess sample solution was removed by a piece of filter paper. Next, the grid was rinsed by 5 μL of water twice. Finally the grid was stained by 5 μL of 2% uranyl acetate solution for 15 s and blotted using a piece of filter paper. The sample was imaged on a JEM-1400 TEM (JEOL) operating at 120 kV.

**CSTET Imaging.** The holey carbon grid (400 mesh, Electron Microscopy Sciences, cat. no. CF424-50) was glow discharged using a PELCO easiGlow glow discharge cleaning system (Ted Pella). The sample was prepared using a Vitrobot Mark IV (FEI) with the temperature of 22 °C, the relative humidity of 100%, the blot force of 0, and the drain time of 0 s. A 5 μL drop of the sample solution was deposited on the holey carbon grid and incubated for 30 s. Then the grid was blotted for 1 s and immediately plunge-frozen in the liquid ethane. The sample was then transferred to a cryo-transfer holder (Gatan) for STEM observation. The images were acquired under the annular dark-field scanning transmission electron microscopy (ADF-STEM) mode in the Talos F200X (FEI).

**CSTET Image Processing and 3D Reconstruction.** The 3D structures were reconstructed from a 10° interval ADF-STEM tomography tilt series using a multiplicative simultaneous iterative reconstruction technique. To remove the elongation artifacts, a particle-support constraint was used in conjunction with a model-based reconstruction algorithm.[25,34,65] The code that implemented these algorithms was custom written in Matlab as part of the TomoIE software package (https://sites.google.com/view/tomoie). The visualization of the reconstructions was rendered using the Avizo software.

**Analysis of Interlayer and Interparticle Distances Based on the Electron Microscopy Images.** The interlayer distances of the pillar (3 + 3), (3 + 4), (3 + 3)*, and (3 + 2) were measured and calculated based on 81, 92, 62, and 18 data points from the negative stained TEM images. Each data point corresponds to the distance between one pair of adjacent layers. The interlayer distances of the pillar (3 + 3) and (3 + 4) were also measured and calculated based on 11 and 10 data points from the 3D reconstructed models. In addition, the interparticle distances of the pillar (3 + 3), cluster A (3 + 4), and


DOI: 10.1021/acsnano.7b02671
ACS Nano XXXX, XXX, XXX−XXX

cluster B (3 + 4) were measured and calculated based on 4, 4, and 3 clusters from the 3D reconstructed models. The clusters that locate at the end of the pillar and only contact one DNA tile were not measured because nanoparticles in those clusters have a larger degree of flexibility.

**Preparation of the Silicon Substrate and Deposition of the Pillars on the Substrate.** For the electron beam lithography, a 1 × 1 $cm^2$ silicon wafer with an 800 nm layer of oxide was ultrasonically cleaned using acetone, rinsed by isopropanol (IPA), and dried with nitrogen gas followed by $O_2$/Ar plasma etching. The pad was fabricated by e-beam lithography, using CRESTEC CABLE-9000C with an emission current of 2 nA and an acceleration voltage of 50 kV. The exposed sample was developed in methyl isobutyl ketone (MIBK)/IPA (1:3) solution for 30 s, submerged in IPA for another 30 s, and dried by nitrogen gas. The wafer was then transferred to the e-beam evaporation chamber (Kurt J Lesker, PVD 75) for deposition of 8 nm-thick Cr, 20 nm-thick Au, and 11 nm-thick Pt. Before the deposition of the sample, the wafer was first cleaned by oxygen plasma (Nordson MARCH, CS-1701). The assembled pillar (3 + 3) (10 $\mu$L) was deposited on the cleaned wafer and incubated in a humid chamber for 10 min. Then the sample was rinsed by ethanol/water (9:1) solution, dried using compressed air, and stored under vacuum.

**Deposition of the Platinum Electrodes.** Regions of high density of the pillars were identified by a SEM incorporated in a DualBeam FIB system (FEI HELIOS 600). The SEM magnification was limited due to charge accumulation on the isolating substrate. Two platinum pads were generated to connect the pads *in situ* to the pillar by FIB-induced deposition. To minimize the potential damage of the pillar, low electron beam current (86 pA) and low accelerating voltage (5 kV) were used. In addition, to avoid a possible effect of platinum scattered from the designated electrodes into the interval between two electrodes, the distance between the deposited platinum electrodes was *ca.* 500 nm.

***I*–*V* Measurement.** The current–voltage measurement was performed using a Signatone CM-170 probe station at ambient temperature. The voltage was swept from −10 to 10 V in steps of 0.1 V with a minimum delay used for measuring the current.

**Preparation and *I*–*V* Measurement of the Control Sample without the Pillar between Platinum Electrodes.** The control sample was prepared in the same way as the sample mentioned above, except that we chose an area without the pillar between two platinum electrodes. This control sample provides the contribution of the buffer, substrate, and *in situ* deposition of platinum electrodes to the conductivity. We used aluminum wire bonding—two bonding on each pad—to connect the pads to a Keithley 6517b Electrometer. To make sure that the bonding was done properly, we measured each pair of bonds; an electric short was observed on each pad, whereas an electric cut off between the pads was clearly demonstrated (Figure S14).

## ASSOCIATED CONTENT

### Supporting Information

The Supporting Information is available free of charge on the ACS Publications website at DOI: 10.1021/acsnano.7b02671.

Supplementary figures, DNA sequences, theoretical models and numerical simulations (PDF)

Movie S1: Reconstructed model Pillar (3 + 3) (AVI)

Movie S2: Reconstructed model Pillar (3 + 3) (AVI)

Movie S3: Reconstructed model Pillar (3 + 4) (AVI)

Movie S4: Reconstructed model Pillar (3 + 4) (AVI)

## AUTHOR INFORMATION

### Corresponding Author

*E-mail: og2226@columbia.edu.

### Notes

The authors declare no competing financial interest.

## ACKNOWLEDGMENTS

This research conducted at the Center for Functional Nanomaterials which is U.S. DOE Office of Science Facilities, operated at Brookhaven National Laboratory under contract no. DE-SC0012704. The authors thank D. Nykypanchuk and Y. Zhang for the help in the SAXS measurement and analysis, F. Camino for assistance in FIB experiments and the work on the probe station, T. Havdala and A. Sharoni for extensive help in preparing the pads on the substrate, and Y. Rabin and D. Porath for helpful discussions. We thank Dr. Jesse Tice of NG Next for the helpful suggestions for the manuscript. The work was supported by BNL LDRD program and NG Next, Northrop Grumman Corporation. L.S. and Y.Y. were supported by the Israel Science Foundation (ISF-164/12) and the German-Israeli Foundation for Scientific Research and Development (GIF) (I-1234-303.10/2014).

## REFERENCES

(1) Fan, J. A.; Wu, C. H.; Bao, K.; Bao, J. M.; Bardhan, R.; Halas, N. J.; Manoharan, V. N.; Nordlander, P.; Shvets, G.; Capasso, F. Self-Assembled Plasmonic Nanoparticle Clusters. *Science* **2010**, *328*, 1135–1138.

(2) Jones, M. R.; Osberg, K. D.; Macfarlane, R. J.; Langille, M. R.; Mirkin, C. A. Templated Techniques for the Synthesis and Assembly of Plasmonic Nanostructures. *Chem. Rev.* **2011**, *111*, 3736–3827.

(3) Barrow, S. J.; Wei, X. Z.; Baldauf, J. S.; Funston, A. M.; Mulvaney, P. The Surface Plasmon Modes of Self-Assembled Gold Nanocrystals. *Nat. Commun.* **2012**, *3*, 1275.

(4) Stebe, K. J.; Lewandowski, E.; Ghosh, M. Oriented Assembly of Metamaterials. *Science* **2009**, *325*, 159–160.

(5) Daniel, M. C.; Astruc, D. Gold Nanoparticles: Assembly, Supramolecular Chemistry, Quantum-Size-Related Properties, and Applications toward Biology, Catalysis, and Nanotechnology. *Chem. Rev.* **2004**, *104*, 293–346.

(6) Rosi, N. L.; Mirkin, C. A. Nanostructures in Biodiagnostics. *Chem. Rev.* **2005**, *105*, 1547–1562.

(7) Nie, Z. H.; Petukhova, A.; Kumacheva, E. Properties and Emerging Applications of Self-Assembled Structures Made from Inorganic Nanoparticles. *Nat. Nanotechnol.* **2010**, *5*, 15–25.

(8) Giljohann, D. A.; Seferos, D. S.; Daniel, W. L.; Massich, M. D.; Patel, P. C.; Mirkin, C. A. Gold Nanoparticles for Biology and Medicine. *Angew. Chem., Int. Ed.* **2010**, *49*, 3280–3294.

(9) Chou, L. Y. T.; Zagorovsky, K.; Chan, W. C. W. DNA Assembly of Nanoparticle Superstructures for Controlled Biological Delivery and Elimination. *Nat. Nanotechnol.* **2014**, *9*, 148–155.

(10) Grzelczak, M.; Vermant, J.; Furst, E. M.; Liz-Marzan, L. M. Directed Self-Assembly of Nanoparticles. *ACS Nano* **2010**, *4*, 3591–3605.

(11) Gao, Y.; Tang, Z. Y. Design and Application of Inorganic Nanoparticle Superstructures: Current Status and Future Challenges. *Small* **2011**, *7*, 2133–2146.

(12) Wang, L. B.; Xu, L. G.; Kuang, H.; Xu, C. L.; Kotov, N. A. Dynamic Nanoparticle Assemblies. *Acc. Chem. Res.* **2012**, *45*, 1916–1926.

(13) Liu, K.; Nie, Z. H.; Zhao, N. N.; Li, W.; Rubinstein, M.; Kumacheva, E. Step-Growth Polymerization of Inorganic Nanoparticles. *Science* **2010**, *329*, 197–200.

(14) Gao, B.; Arya, G.; Tao, A. R. Self-Orienting Nanocubes for the Assembly of Plasmonic Nanojunctions. *Nat. Nanotechnol.* **2012**, *7*, 433–437.

(15) Stupp, S. I.; Palmer, L. C. Supramolecular Chemistry and Self-Assembly in Organic Materials Design. *Chem. Mater.* **2014**, *26*, 507–518.

(16) Webber, M. J.; Appel, E. A.; Meijer, E. W.; Langer, R. Supramolecular Biomaterials. *Nat. Mater.* **2016**, *15*, 13–26.



DOI: 10.1021/acsnano.7b02671
*ACS Nano* XXXX, XXX, XXX–XXX

(17) Mirkin, C. A.; Letsinger, R. L.; Mucic, R. C.; Storhoff, J. J. A DNA-Based Method for Rationally Assembling Nanoparticles into Macroscopic Materials. *Nature* **1996**, *382*, 607−609.
(18) Alivisatos, A. P.; Johnsson, K. P.; Peng, X. G.; Wilson, T. E.; Loweth, C. J.; Bruchez, M. P.; Schultz, P. G. Organization of 'Nanocrystal Molecules' Using DNA. *Nature* **1996**, *382*, 609−611.
(19) Nykypanchuk, D.; Maye, M. M.; van der Lelie, D.; Gang, O. DNA-Guided Crystallization of Colloidal Nanoparticles. *Nature* **2008**, *451*, 549−552.
(20) Park, S. Y.; Lytton-Jean, A. K. R.; Lee, B.; Weigand, S.; Schatz, G. C.; Mirkin, C. A. DNA-Programmable Nanoparticle Crystallization. *Nature* **2008**, *451*, 553−556.
(21) Macfarlane, R. J.; Lee, B.; Jones, M. R.; Harris, N.; Schatz, G. C.; Mirkin, C. A. Nanoparticle Superlattice Engineering with DNA. *Science* **2011**, *334*, 204−208.
(22) Zhang, C.; Macfarlane, R. J.; Young, K. L.; Choi, C. H. J.; Hao, L. L.; Auyeung, E.; Liu, G. L.; Zhou, X. Z.; Mirkin, C. A. A General Approach to DNA-Programmable Atom Equivalents. *Nat. Mater.* **2013**, *12*, 741−746.
(23) Zhang, Y. G.; Lu, F.; Yager, K. G.; van der Lelie, D.; Gang, O. A General Strategy for the DNA-Mediated Self-Assembly of Functional Nanoparticles into Heterogeneous Systems. *Nat. Nanotechnol.* **2013**, *8*, 865−872.
(24) Estephan, Z. G.; Qian, Z. X.; Lee, D.; Crocker, J. C.; Park, S. J. Responsive Multidomain Free-Standing Films of Gold Nanoparticles Assembled by DNA-Directed Layer-by-Layer Approach. *Nano Lett.* **2013**, *13*, 4449−4455.
(25) Lu, F.; Yager, K. G.; Zhang, Y. G.; Xin, H. L.; Gang, O. Superlattices Assembled through Shape-Induced Directional Binding. *Nat. Commun.* **2015**, *6*, 6912.
(26) O'Brien, M. N.; Jones, M. R.; Lee, B.; Mirkin, C. A. Anisotropic Nanoparticle Complementarity in DNA-Mediated Co-Crystallization. *Nat. Mater.* **2015**, *14*, 833−840.
(27) Lin, H.; Lee, S.; Sun, L.; Spellings, M.; Engel, M.; Glotzer, S. C.; Mirkin, C. A. Clathrate Colloidal Crystals. *Science* **2017**, *355*, 931−935.
(28) Ding, B. Q.; Deng, Z. T.; Yan, H.; Cabrini, S.; Zuckermann, R. N.; Bokor, J. Gold Nanoparticle Self-Similar Chain Structure Organized by DNA Origami. *J. Am. Chem. Soc.* **2010**, *132*, 3248−3249.
(29) Pal, S.; Deng, Z. T.; Ding, B. Q.; Yan, H.; Liu, Y. DNA-Origami-Directed Self-Assembly of Discrete Silver-Nanoparticle Architectures. *Angew. Chem., Int. Ed.* **2010**, *49*, 2700−2704.
(30) Zhang, C.; Li, X.; Tian, C.; Yu, G. M.; Li, Y. L.; Jiang, W.; Mao, C. D. DNA Nanocages Swallow Gold Nanoparticles (AuNPs) to Form AuNP@DNA Cage Core-Shell Structures. *ACS Nano* **2014**, *8*, 1130−1135.
(31) Schreiber, R.; Do, J.; Roller, E. M.; Zhang, T.; Schuller, V. J.; Nickels, P. C.; Feldmann, J.; Liedl, T. Hierarchical Assembly of Metal Nanoparticles, Quantum Dots and Organic Dyes Using DNA Origami Scaffolds. *Nat. Nanotechnol.* **2014**, *9*, 74−78.
(32) Samanta, A.; Deng, Z. T.; Liu, Y. Infrared Emitting Quantum Dots: DNA Conjugation and DNA Origami Directed Self-Assembly. *Nanoscale* **2014**, *6*, 4486−4490.
(33) Roller, E. M.; Khorashad, L. K.; Fedoruk, M.; Schreiber, R.; Govorov, A. O.; Liedl, T. DNA-Assembled Nanoparticle Rings Exhibit Electric and Magnetic Resonances at Visible Frequencies. *Nano Lett.* **2015**, *15*, 1368−1373.
(34) Tian, Y.; Wang, T.; Liu, W. Y.; Xin, H. L.; Li, H. L.; Ke, Y. G.; Shih, W. M.; Gang, O. Prescribed Nanoparticle Cluster Architectures and Low-Dimensional Arrays Built Using Octahedral DNA Origami Frames. *Nat. Nanotechnol.* **2015**, *10*, 637−645.
(35) He, L. C.; Mao, C. C.; Cho, S.; Ma, K.; Xi, W. X.; Bowman, C. N.; Park, W.; Cha, J. N. Experimental and Theoretical Photoluminescence Studies in Nucleic Acid Assembled Gold-Upconverting Nanoparticle Clusters. *Nanoscale* **2015**, *7*, 17254−17260.
(36) Urban, M. J.; Dutta, P. K.; Wang, P. F.; Duan, X. Y.; Shen, X. B.; Ding, B. Q.; Ke, Y. G.; Liu, N. Plasmonic Toroidal Metamolecules Assembled by DNA Origami. *J. Am. Chem. Soc.* **2016**, *138*, 5495−5498.
(37) Kuzyk, A.; Schreiber, R.; Zhang, H.; Govorov, A. O.; Liedl, T.; Liu, N. Reconfigurable 3D Plasmonic Metamolecules. *Nat. Mater.* **2014**, *13*, 862−866.
(38) Lo, P. K.; Karam, P.; Aldaye, F. A.; McLaughlin, C. K.; Hamblin, G. D.; Cosa, G.; Sleiman, H. F. Loading and Selective Release of Cargo in DNA Nanotubes with Longitudinal Variation. *Nat. Chem.* **2010**, *2*, 319−328.
(39) Liu, W. Y.; Halverson, J.; Tian, Y.; Tkachenko, A. V.; Gang, O. Self-Organized Architectures from Assorted DNA-Framed Nanoparticles. *Nat. Chem.* **2016**, *8*, 867−873.
(40) Schreiber, R.; Santiago, I.; Ardavan, A.; Turberfield, A. J. Ordering Gold Nanoparticles with DNA Origami Nanoflowers. *ACS Nano* **2016**, *10*, 7303−7306.
(41) Gur, F. N.; Schwarz, F. W.; Ye, J. J.; Diez, S.; Schmidt, T. L. Toward Self-Assembled Plasmonic Devices: High-Yield Arrangement of Gold Nanoparticles on DNA Origami Templates. *ACS Nano* **2016**, *10*, 5374−5382.
(42) Sharma, J.; Chhabra, R.; Cheng, A.; Brownell, J.; Liu, Y.; Yan, H. Control of Self-Assembly of DNA Tubules through Integration of Gold Nanoparticles. *Science* **2009**, *323*, 112−116.
(43) Kuzyk, A.; Schreiber, R.; Fan, Z. Y.; Pardatscher, G.; Roller, E. M.; Hogele, A.; Simmel, F. C.; Govorov, A. O.; Liedl, T. DNA-Based Self-Assembly of Chiral Plasmonic Nanostructures with Tailored Optical Response. *Nature* **2012**, *483*, 311−314.
(44) Sharma, J.; Chhabra, R.; Liu, Y.; Ke, Y. G.; Yan, H. DNA-Templated Self-Assembly of Two-Dimensional and Periodical Gold Nanoparticle Arrays. *Angew. Chem., Int. Ed.* **2006**, *45*, 730−735.
(45) Zhang, J. P.; Liu, Y.; Ke, Y. G.; Yan, H. Periodic Square-Like Gold Nanoparticle Arrays Templated by Self-Assembled 2D DNA Nanogrids on a Surface. *Nano Lett.* **2006**, *6*, 248−251.
(46) Zheng, J. W.; Constantinou, P. E.; Micheel, C.; Alivisatos, A. P.; Kiehl, R. A.; Seeman, N. C. Two-Dimensional Nanoparticle Arrays Show the Organizational Power of Robust DNA Motifs. *Nano Lett.* **2006**, *6*, 1502−1504.
(47) Ke, Y. G.; Ong, L. L.; Sun, W.; Song, J.; Dong, M. D.; Shih, W. M.; Yin, P. DNA Brick Crystals with Prescribed Depths. *Nat. Chem.* **2014**, *6*, 994−1002.
(48) Wang, P. F.; Gaitanaros, S.; Lee, S.; Bathe, M.; Shih, W. M.; Ke, Y. G. Programming Self-Assembly of DNA Origami Honeycomb Two-Dimensional Lattices and Plasmonic Metamaterials. *J. Am. Chem. Soc.* **2016**, *138*, 7733−7740.
(49) Sharma, J.; Ke, Y. G.; Lin, C. X.; Chhabra, R.; Wang, Q. B.; Nangreave, J.; Liu, Y.; Yan, H. DNA-Tile-Directed Self-Assembly of Quantum Dots into Two-Dimensional Nanopatterns. *Angew. Chem., Int. Ed.* **2008**, *47*, 5157−5159.
(50) Hung, A. M.; Micheel, C. M.; Bozano, L. D.; Osterbur, L. W.; Wallraff, G. M.; Cha, J. N. Large-Area Spatially Ordered Arrays of Gold Nanoparticles Directed by Lithographically Confined DNA Origami. *Nat. Nanotechnol.* **2010**, *5*, 121−126.
(51) Lin, C. X.; Liu, Y.; Rinker, S.; Yan, H. DNA Tile Based Self-Assembly: Building Complex Nanoarchitectures. *ChemPhysChem* **2006**, *7*, 1641−1647.
(52) Tian, C.; Li, X.; Liu, Z. Y.; Jiang, W.; Wang, G. S.; Mao, C. D. Directed Self-Assembly of DNA Tiles into Complex Nanocages. *Angew. Chem., Int. Ed.* **2014**, *53*, 8041−8044.
(53) Rothemund, P. W. K. Folding DNA to Create Nanoscale Shapes and Patterns. *Nature* **2006**, *440*, 297−302.
(54) Ke, Y. G.; Ong, L. L.; Shih, W. M.; Yin, P. Three-Dimensional Structures Self-Assembled from DNA Bricks. *Science* **2012**, *338*, 1177−1183.
(55) Mohammed, A. M.; Šulc, P.; Zenk, J.; Schulman, R. Self-Assembling DNA Nanotubes to Connect Molecular Landmarks. *Nat. Nanotechnol.* **2017**, *12*, 312−316.
(56) Yao, G. B.; Li, J.; Chao, J.; Pei, H.; Liu, H. J.; Zhao, Y.; Shi, J. Y.; Huang, Q.; Wang, L. H.; Huang, W.; Fan, C. H. Gold-Nanoparticle-Mediated Jigsaw-Puzzle-Like Assembly of Supersized Plasmonic DNA Origami. *Angew. Chem., Int. Ed.* **2015**, *54*, 2966−2969.


DOI: 10.1021/acsnano.7b02671
*ACS Nano* XXXX, XXX, XXX−XXX

(57) Lan, X.; Lu, X. X.; Shen, C. Q.; Ke, Y. G.; Ni, W. H.; Wang, Q. B. Au Nanorod Helical Superstructures with Designed Chirality. *J. Am. Chem. Soc.* **2015**, *137*, 457−462.
(58) Ko, S. H.; Gallatin, G. M.; Liddle, J. A. Nanomanufacturing with DNA Origami: Factors Affecting the Kinetics and Yield of Quantum Dot Binding. *Adv. Funct. Mater.* **2012**, *22*, 1015−1023.
(59) Narayan, K.; Subramaniam, S. Focused Ion Beams in Biology. *Nat. Methods* **2015**, *12*, 1021−1031.
(60) Bockrath, M.; Cobden, D. H.; Lu, J.; Rinzler, A. G.; Smalley, R. E.; Balents, L.; McEuen, P. L. Luttinger-Liquid Behaviour in Carbon Nanotubes. *Nature* **1999**, *397*, 598−601.
(61) Bachtold, A.; de Jonge, M.; Grove-Rasmussen, K.; McEuen, P. L.; Buitelaar, M.; Schonenberger, C. Suppression of Tunneling into Multiwall Carbon Nanotubes. *Phys. Rev. Lett.* **2001**, *87*, 166801.
(62) Aleshin, A. N.; Lee, H. J.; Park, Y. W.; Akagi, K. One-Dimensional Transport in Polymer Nanofibers. *Phys. Rev. Lett.* **2004**, *93*, 196601.
(63) Chen, G. F.; Mao, C. D. Long Conducting Polymer Nanonecklaces with a 'Beads-on-a-String' Morphology: DNA Nanotube-Template Synthesis and Electrical Properties. *Nanoscale* **2016**, *8*, 10026−10029.
(64) Kim, K. H.; Lara-Avila, S.; Kang, H.; He, H.; Eklof, J.; Hong, S. J.; Park, M.; Moth-Poulsen, K.; Matsushita, S.; Akagi, K.; Kubatkin, S.; Park, Y. W. Apparent Power Law Scaling of Variable Range Hopping Conduction in Carbonized Polymer Nanofibers. *Sci. Rep.* **2016**, *6*, 37783.
(65) Li, J. C.; Su, D.; Xin, H. L. A Model Based Method for Tomographic Reconstructions of Nanoparticle Assemblies. *Microsc. Microanal.* **2014**, *20*, 808−809.



DOI: 10.1021/acsnano.7b02671
*ACS Nano* XXXX, XXX, XXX−XXX